Wide-Field and Real-Time Super-Resolution Optical Imaging By Titanium Dioxide Nanoparticle-Assembled Solid Immersion Lens

Wang, Weicheng; Yan, Bing; Wang, Haiyan; Chen, Yue; Nie, Xiuyu; Yi, Changfeng; Wang, Zengbo (James); Xu, Zushun; Zeng, Jing; Fan, Wen

Small

28. Apr. 2024

Wide-Field and Real-Time Super-Resolution Optical Imaging By Titanium Dioxide Nanoparticle-Assembled Solid Immersion Lens

Weicheng Wang, Bing Yan, Haiyan Wang, Yue Chen, Xiuyu Nie, Changfeng Yi,Zengbo Wang, Zushun Xu,* Jing Zeng,* and Wen Fan*

Super-resolution optical imaging techniques can break the optical diffrac-tion limit, thus providing unique opportunities to visualize the micro-scopic world at the nanoscale. Although near-field optical microscopytechniques have been proven to achieve significantly improved imagingresolution, most near-field approaches still suffer from a narrow fieldof view (FOV) or difficulty in obtaining wide-field images in real time,which may limit their widespread and diverse applications. Here, theauthors experimentally demonstrate an optical microscope magnificationand image enhancement approach by using a submillimeter-sized solidimmersion lens (SIL) assembled by densely-packed 15 nm TiO$_2$ nano-particles through a silicone oil two-step dehydration method. This TiO$_2$nanoparticle-assembled SIL can achieve both high transparency and highrefractive index, as well as sufficient mechanical strength and easy-to-handle size, thus providing a fast, wide-field, real-time, non-destructive,and low-cost solution for improving the quality of optical microscopicobservation of a variety of samples, including nanomaterials, cancer cells,and living cells or bacteria under conventional optical microscopes. Thisstudy provides an attractive alternative to simplify the fabrication andapplications of high-performance SILs.

W. Wang, H. Wang, Y. Chen, X. Nie, C. Yi, Z. Xu, W. Fan
Ministry of Education Key Laboratory for the Green Preparation
and Application of Functional Materials
Hubei Key Laboratory of Polymer Materials
School of Materials Science and Engineering
Hubei University
Wuhan 430062, P. R. China
E-mail: zushunxu@hubu.edu.cn; fanwen@hubu.edu.cn
B. Yan, Z. Wang
School of Computer Science and Electronic Engineering
Bangor University
Bangor LL57 1UT, UK
J. Zeng
Department of Materials Science and State Key Laboratory of Molecular
Engineering of Polymers
Fudan University
Shanghai 200433, P. R. China
E-mail: jingzeng@alu.fudan.edu.cn

1. Introduction

Optical microscope, with its ability to magnify and visualize small objects invisible to the naked eye, is widely used in a variety of scientific and industrial fields, including biology, medicine, physics, semiconductor manufacturing, and material science.[1–7] However, the maximum image resolution of conventional optical microscopes can only reach approximately half the wavelength of the illuminated visible light, that is, 200 nm, because of the diffraction limit of light.[8] This makes it increasingly challenging to meet the ever-growing demands in nanotechnology and nanomedicine for optical microscopic observations at the nanoscale.

To achieve super-resolution imaging of sub-wavelength nanostructures, several innovative techniques have been developed to break the diffraction barrier in either far-field or near-field regions.[9] For example, super-resolution fluorescence microscopy techniques such as stimulated emission depletion (STED) microscopy and photoactivated localization microscopy (PALM), can increase the resolving power of microscopes to 20–50 nm by reducing or avoiding the diffraction effects of far-field propagating waves.[10,11] However, these fluorescence far-field approaches mainly rely on the use of fluorescent probes and are not suitable for imaging non-fluorescent objects.[12]

In the near-field approaches, such as near-field scanning optical microscopy (NSOM),[13–16] silver slab superlens,[17–19] micro-sphere superlens,[20–22] and metamaterial solid immersion lenses (SIL),[23,24] different optics including scanning probes, metallic slab, dielectric microspheres or nanoparticles have been designed to sufficiently approach and capture the near-field evanescent waves that carry sub-diffraction limit information about an object but decay exponentially with distance from the object surface, thus enabling a resolution of around 50 nm to be achieved.

Nevertheless, these techniques still suffer from some limita-tions that hinder their widespread applications. For example, NSOM requires time-consuming scanning of the field of view (FOV), which limits the potential for real-time and dynamic imaging.[9] On the other hand, the imaging plane of silver slab

superlens is limited to the near-field due to the rapid attenuation of evanescent waves transmitted through the silver layer.[17] Moreover, although silver-based hyperbolic superlens can convert evanescent waves into far-field propagating waves under UV illumination, the intrinsic metallic loss may limit their performance and applications at visible wavelengths.[18,25,26] Owing to the ability to project the near-field information into magnified far-field images, transparent dielectric microspheres have been demonstrated to be a simple and effective approach for the observation of sub-diffraction structures of various nanomaterials and even adenovirus nanoparticles under a conventional white light microscope.[20,27–32] But one drawback is that the microsphere superlens often suffers from a narrow FOV because the super-resolution capability is only significant in relatively small microspheres with diameters ranging from several microns to tens of microns.[21] In addition, such a small size greatly increases the difficulty of precise positioning and manipulation of an individual microsphere superlens in order to image a specific region of a sample.

Solid immersion lens (SIL) uses a truncated solid sphere with a high refractive index and transparency to fill the space between the objective lens of a light microscope and the sample surface, thereby can improve the light-collection efficiency, numerical aperture (NA), as well as the spatial resolution of the objective lens.[33–36] Conventional SIL is fabricated from homogeneous materials such as high-refractive-index glass or diamond.[35] We have ever reported a nano-solid-fluid method to assemble 15 nm TiO_2 nanoparticles into a 20 µm-wide metamaterial SIL, which achieved a record-breaking superlens resolution of 45 nm under a white light microscope.[23] Owing to the densely packed structure of anatase TiO_2 nanoparticles with a refractive index of 2.55, the metamaterial SIL has achieved both high transparency and a highly effective refractive index approaching 2.0, and can efficiently collect and convert the near-field evanescent information into far-field propagating waves.[23] However, the limited size of this metamaterial SIL restricts its FOV and also reduces its operability.

Until now, most SIL manufacturing technologies rely on costly and complex top-down methods, such as electron-beam lithography and focussed ion beam milling.[33–35] The design and fabrication of polymer SIL are relatively simple and cost-effective, but the low refractive index (typically below 1.6) of polymer material limits the optical and imaging performance of the SIL.[37] Here, we report a bottom-up silicone oil two-step dehydration method to successfully assemble high refractive index, low absorption loss, and deep-subwavelength scale 15 nm anatase TiO_2 nanoparticles into TiO_2 SIL for wide-field and real-time microscopic super-resolution imaging of a variety of samples including nanomaterials and stained or unstained biological cells under conventional white light microscopes. This TiO_2 nanoparticle-assembled SIL will be useful to extend the current solid immersion techniques.

2. Results and Discussion

2.1. The Self-Assembly of TiO₂ SIL

The bottom-up self-assembly technique provides a facile and versatile route to fabricate novel optical devices. However, during the self-assembly process of nanomaterial building blocks such as nanoparticles, irreversible particle aggregation, and drying shrinkage cracking often occur and lead to structural defects including air voids and cracks with feature sizes comparable to even larger than visible wavelengths. These microscopic defects can cause significant optical scattering loss, especially for high-refractive-index materials, which seriously affects the optical transparency and final performance of the fabricated optical devices. Therefore, in order to assemble TiO_2 nanoparticles into an optically transparent SIL with high transmittance in the visible region, it is necessary to use TiO_2 nanoparticles with sizes much smaller than the visible wavelength, and also to assemble these deep-subwavelength nanoparticles into the densely packed and defect-free structure.

The present silicone oil two-step dehydration method utilizes the immiscibility of silicone oil and water, as well as the high boiling point (non-volatile) and low surface tension (lubricity) of silicone oil, to assemble TiO_2 nanoparticles into regular hemispherical microlenses with high refractive index, high transparency, and easy-to-handle size of hundreds of microns.

Figure 1 shows the schematic diagram of the assembly process of the TiO_2 SIL by the silicone oil two-step dehydration method, which mainly consists of two successive dehydration steps. In brief, a piece of hydrophobic polycarbonate film is placed on the bottom surface of a container such as a Petri dish filled with low-viscosity silicone oil. Then, a small volume of aqueous dispersion of 15 nm TiO_2 nanoparticles is added to the silicone oil using a pipette. Because the density of water is slightly greater than that of silicone oil, the aqueous droplet of TiO_2 nanoparticles is deposited on the polycarbonate surface and deformed into a hemispherical shape under the combined action of silicone oil/water interfacial tension and gravity (Figure 1a). Subsequently, the silicone oil is heated at 70 °C for 1–2 h depending on the volume of the aqueous droplet, and therefore part of the water in the aqueous droplet can be evaporated away from the silicone oil/water interface. This first step of dehydration decreases the volume of the aqueous droplet and the interparticle distance between TiO_2 nanoparticles (Figure S1, Supporting Information). When the TiO_2 nanoparticles are forced to approach each other within a certain distance, the electrostatic repulsion between the positively charged (+27 mV) TiO_2 nanoparticles becomes significant due to the overlapping of the electrostatic repulsion layers of adjacent TiO_2 nanoparticles, which is expected to restrict the mobility of particles in a limited space and cause an unjamming-to-jamming transition of TiO_2 nanoparticles. Correspondingly, the aqueous droplet will undergo a phase transition from a fluid state to a gel-like semisolid state. By the first step of dehydration, the ideal hemispherical shape of the SIL can be appropriately fixed.

The second step of dehydration is carried out at a room temperature of 25 °C for 24 h. After removing the silicone oil from the Petri dish, a thin layer of residual silicone oil can still cover the surface of the gel-like hemispherical droplet due to the low surface tension and lubricating properties of silicone oil (Figure 1b). This silicone oil layer can act as a protective shell at the hemispherical droplet boundary to allow the gradual evaporation of residual water in the interstices of the TiO_2 nanoparticles. Finally, interparticle capillary and van der Waals attractive forces during the dying process are capable of making nanoparticles
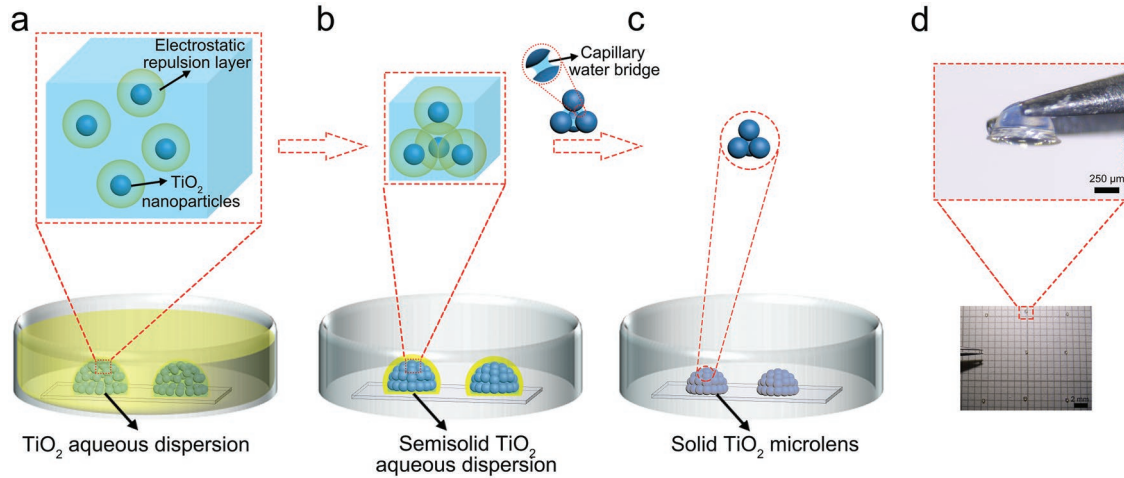
Figure 1. The schematic diagram of the assembly process of the TiO$_2$ SIL by the silicone oil two-step dehydration method. a) The first step of dehydration is achieved by partially evaporating the hemispherical-shaped aqueous droplet containing TiO$_2$ nanoparticles in hot silicone oil to form a semisolid droplet. b) The second step of dehydration is achieved by completely evaporating the residual water between the TiO$_2$ nanoparticles in ambient air to form solid microlens. c) The schematic and d) representative photographs of the TiO$_2$ SIL assembled by tightly packed TiO$_2$ nanoparticles.

come in close contact with each other (Figure 1c), leading to a TiO$_2$ solid microlens with a smooth hemispherical shape and high optical transparency under visible light. The residual silicone oil on the surface of the microlens can be further removed by wicking with bibulous paper or rinsing with organic solvent (e.g., hexane). The fabricated TiO$_2$ SIL has sufficient mechanical strength for practical use (Figure S2, Supporting Information) and submillimeter sizes that are directly visible to the naked eye, thereby can be easily picked up individually and transferred to a target surface using a sharp tweezer, as shown in Figure 1d.

Additionally, the morphological features such as the width and height-width ratio of the TiO$_2$ SIL can be controlled by adjusting parameters including the volume of the TiO$_2$ aqueous droplet and the surface hydrophobicity of the underlying substrate placed in the Petri dish. For example, the sequence of adding silicone oil and TiO$_2$ aqueous droplet on the polycarbonate substrate influences the droplet shape. A hemispherical TiO$_2$ SIL can be formed when a TiO$_2$ aqueous droplet is first added to the polycarbonate substrate before the addition of silicone oil. While pre-wetting of the polycarbonate substrate with silicone oil before adding a TiO$_2$ aqueous droplet enables better water repellency of the polycarbonate surface, leading to a higher height-width ratio of the oil-suspended TiO$_2$ aqueous droplet and the subsequently formed super-hemispherical TiO$_2$ SIL with a height-width ratio larger than 0.6. Using a fluorinated ethylene propylene (FEP) film with a superhydrophobic surface, a spherical TiO$_2$ microlens with a height-width ratio approaching unity can be assembled (Figure S3, Supporting Information). Moreover, the TiO$_2$ SILs assembled by this method exhibit good repeatability in their geometry and optical properties (Figure S4, Supporting Information).

2.2. Factors Affecting the Magnification Factor and FOV of TiO$_2$ SIL

The magnification factor and FOV of the TiO$_2$ SIL are two important indicators to evaluate its imaging performance.

Here, a stage micrometer with 10 µm divisions was used as a test object and imaged under a white-light transmission optical microscope using a 10× objective lens (Numerical aperture, NA = 0.25), as shown in **Figure 2**. Figure 2a shows that the stage micrometer has parallel line patterns with line widths of 3.75 µm and spacings of 10 µm. Figure 2b–d shows the overall imaging performance of the TiO$_2$ SIL with hemispherical, super-hemispherical, and spherical shapes. The hemispherical SIL has a height-width ratio of 0.532 and a width of 413 µm, and the corresponding magnification factor and FOV are 2.3 and 8833 µm^2, respectively (Figure 2b). The super-hemispherical SIL with a height-width ratio of 0.689 and a width of 369 µm has a magnification factor of 3.5 and a FOV of 7220 µm^2 (Figure 2c). The spherical microlens with a height-width ratio of 1 and a width of 379 µm cannot provide magnified images in air (Figure 2d). However, by encapsulating the spherical microlens into a polydimethylsiloxane (PDMS) layer with a thickness of 591 µm, an imaging magnification of 2.9× and a FOV of 5896 µm^2 can be realized (Figure 2e).

It is further demonstrated that the magnification factor depends mainly on the height-width ratio of the SIL, and has little relationship with the SIL width. On the other hand, the FOV is proportional to the SIL width and less related to the height-width ratio of the SIL. As shown in Figure 2f–w, the six sets of vertically aligned SIL have a fixed height-width ratio of 0.52, 0.59, 0.65, 0.67, 0.68, and 0.69, respectively. Their corresponding magnification factors are 2.2, 2.4, 2.9, 3.2, 3.3, and 3.6, respectively. The plots in Figure 2x suggest that the magnification factor increases sharply when the height-width ratio tends to approach 0.7. Additionally, the three sets of horizontally arranged SIL have similar widths of about 379, 464, and 631 µm, respectively. Their corresponding imaging FOV are about 7486, 13085, and 25237 µm^2, respectively. It is apparent that the FOV (undistorted region) increases linearly with an increase in the SIL width (Figure 2y).

These TiO$_2$ SILs with a width below 650 µm and a height-width ratio below 0.7 have universal applicability under
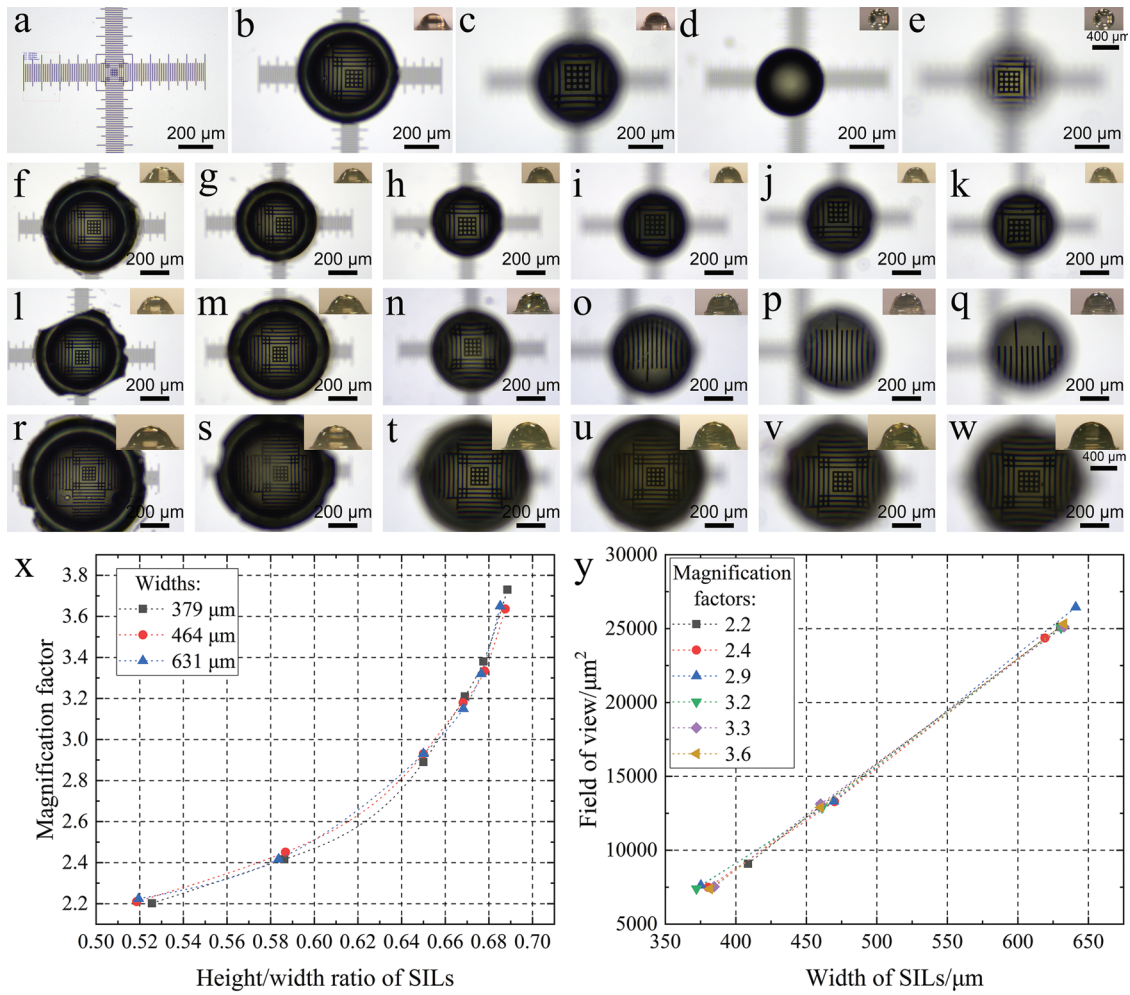
Figure 2. Investigation of the magnification factor and FOV of the TiO$_2$ SIL under a transmission optical microscope with a 10× objective lens. a) Direct observation of the line patterns with 10 μm spacing on a stage micrometer. b–e) Typical optical micrographs observed by hemispherical, super-hemispherical, spherical, and PDMS-encapsulated spherical TiO$_2$ microlens, respectively. f–w) Optical micrographs observed by TiO$_2$ SILs with different widths (around 379, 464, and 631 μm for the three horizontal sets, respectively) and height-width ratios (around 0.52, 0.59, 0.65, 0.67, 0.68, and 0.69 for the six vertical sets, respectively). The insets in (b–w) show the corresponding side-views of the TiO$_2$ microlenses observed by a stereo-optical microscope. x) A plot of the imaging magnification factor as a function of the height-width ratio of the TiO$_2$ SIL with different widths. y) A plot of the imaging FOV as a function of the width of TiO$_2$ SIL with different magnification factors.

different microscope conditions. For example, they also have a suitable size to fit and focus within the short working distance of a high magnification/NA air objective lens down to 0.66 mm (Figure S5, Supporting Information). It is noteworthy that the magnification factor of a TiO$_2$ SIL is determined by the microlens itself, rather than by the microscope objective or microscope type used (Figure S6, Supporting Information). Furthermore, it was found that the centering of the focused light spot of the microscope on the TiO$_2$ SIL is important to obtain the optimal SIL image quality when using a high magnification/NA objective lens (Figure S7, Supporting Information).

2.3. Super-Resolution Performance of TiO$_2$ SIL

To investigate the super-resolution imaging performance of the TiO$_2$ SIL, a monolayer of monodisperse SiO$_2$ or polystyrene

(PS) nanospheres with a diameter of 400 or 300 nm was respectively assembled onto a PDMS substrate, and observed through a TiO$_2$ SIL under a transmission or reflection optical microscope at different microscopic illumination conditions, as shown in **Figure 3**. The scanning electron microscopy (SEM) images indicate that the monolayer of nanospheres is packed in a close-packed hexagonal array in the 400 nm (Figure 3a) and 300 nm (Figure 3k) nanosphere samples, respectively.

Under direct microscopic observation by a transmission optical microscope using a 40× objective lens, the nanocrystalline structures in the 400 nm nanosphere array cannot be resolved in either bright-field vertical illumination (Figure 3b) or dark-field oblique illumination (Figure 3d). Figures 3c and 3e are the partially enlarged views of the regions inside the red boxes in Figures 3b and 3d, respectively, revealing that only the gaps between the grain boundaries are observed. According to the Rayleigh criterion for resolving two-point
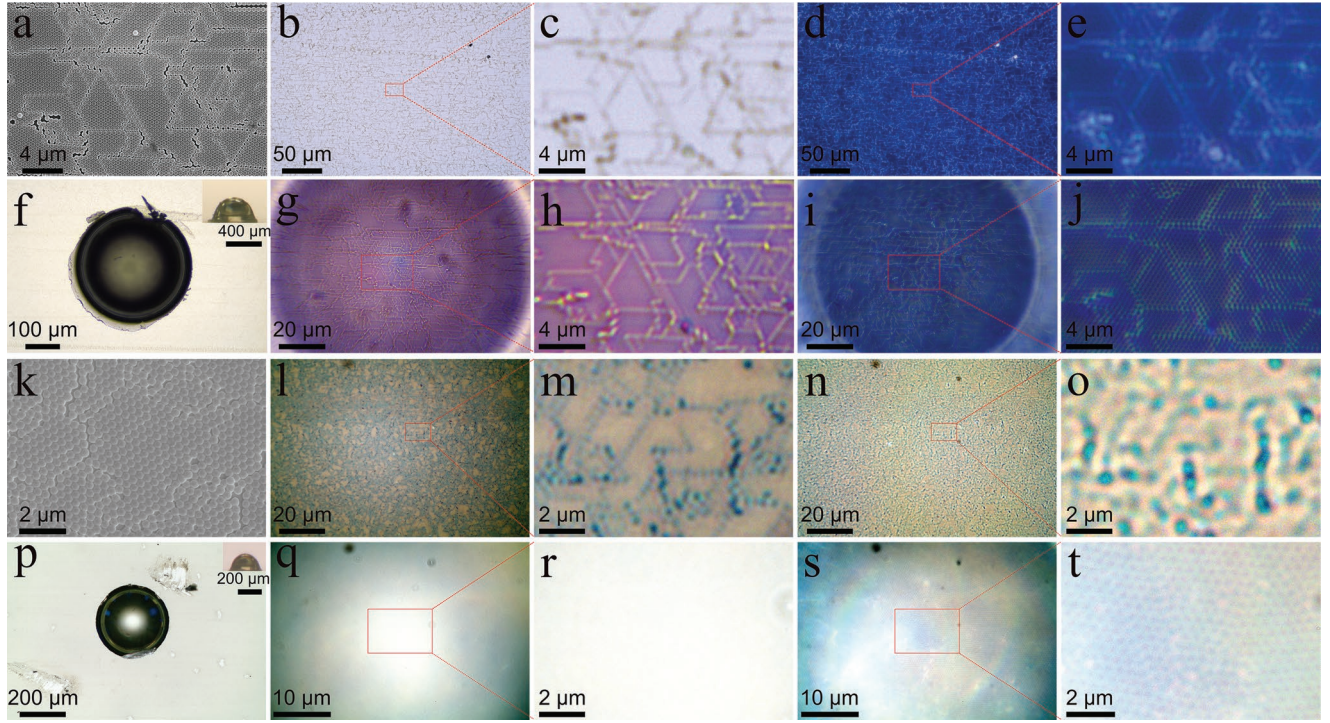
Figure 3. Evaluation of the super-resolution performance of the TiO$_2$ SIL. a,k) SEM images of 400 and 300 nm nanosphere arrays, respectively. f,p) Optical micrographs of the top and side views of the TiO$_2$ SIL with a width of 446 µm and a height-width ratio of 0.638, and a width of 223 µm and a height-width ratio of 0.613, respectively located at the 400 and 300 nm nanosphere arrays. b–e) Optical micrographs of the 400 nm nanosphere array observed using a transmission optical microscope equipped with a 40× objective lens (NA = 0.75) in b) bright-field vertical illumination or d) dark-field oblique illumination mode, where (c) and (e) are the partially enlarged images of (b) and (d), respectively. g–j) Corresponding optical micrographs of the 400 nm nanosphere array observed through the TiO$_2$ SIL in g) bright-field vertical illumination or i) dark-field oblique illumination mode, where (h) and (j) are the partially enlarged images of (g) and (i), respectively. l–o) Optical micrographs of the 300 nm nanosphere array observed using a reflection optical microscope equipped with a 100× objective lens (NA = 0.9) in l) bright-field vertical illumination or n) bright-field oblique illumination mode, where (m) and (o) are the partially enlarged images of (l) and (n), respectively. q–t) Corresponding optical micrographs of the 300 nm nanosphere array observed through the TiO$_2$ SIL in q) bright-field vertical illumination or s) bright-field oblique illumination mode, where (r) and (t) are the partially enlarged images of (q) and (s), respectively.

sources, the limited resolution of the 40× objective lens can be estimated as $0.61\lambda/NA \approx 447$ nm, where $NA = 0.75$, $\lambda = 550$ nm is the average wavelength of white light. This suggests that the resolving power of the 40× objective lens is not sufficient to distinguish an individual nanosphere.

When a TiO$_2$ SIL with a width of 446 µm and a height-width ratio of 0.638 was transferred to the surface of the nanosphere array (Figure 3f), the optical resolution of the 2.9× magnified image seems to be improved under the bright-field vertical illumination, but it is still difficult to identify the periodicity and spacing of the nanospheres, as shown in Figure 3g and the local enlargement in Figure 3h. However, in the dark-field oblique illumination mode, the hexagonal lattice structure of the nanospheres can be clearly distinguished by the TiO$_2$ SIL, as shown in Figure 3i and the local enlargement in Figure 3j. It has been previously demonstrated that compared to vertical illumination, oblique illumination can improve the imaging resolution and contrast of hemispherical or spherical superlens.[21,23] Here, by using dark-field illumination, the TiO$_2$ SIL can also be illuminated by oblique incident light, thus enhancing the imaging quality of the TiO$_2$ SIL.

The TiO$_2$ SIL is also capable of producing super-resolution images under reflected illumination. Under the direct observation of a metallographic optical microscope equipped with a 100× objective lens (NA = 0.9), the nano-periodic structures in the 300 nm nanosphere array could not be resolved under both bright-field vertical illumination (Figure 3l) and bright-field oblique illumination (Figure 3n). These are shown more clearly in the enlargement of Figure 3m,o, respectively. Similarly, the theoretical resolution of the 100× objective lens is about 373 nm according to the Rayleigh criterion, which is essentially unable to distinguish the fine structure of the nanoarray.

When a TiO$_2$ SIL with a width of 223 µm and a height-width ratio of 0.613 was transferred to the surface of the nanosphere array (Figure 3p), the nano-periodic structure is still not clearly resolved under the bright-field illumination, as shown in Figure 3q and its partially enlarged view in Figure 3r. The image captured through the TiO$_2$ SIL was overexposed, probably because the existence of an air gap between the SIL and the sample surface increased the light scattering effect, resulting in an opaque appearance. However, when observed under bright-field oblique illumination, the light scattering effect can be suppressed, thus the regular hexagonal lattice structure was clearly observed through the 2.5× magnified image, as shown in Figure 3s and the corresponding enlarged image in Figure 3t.
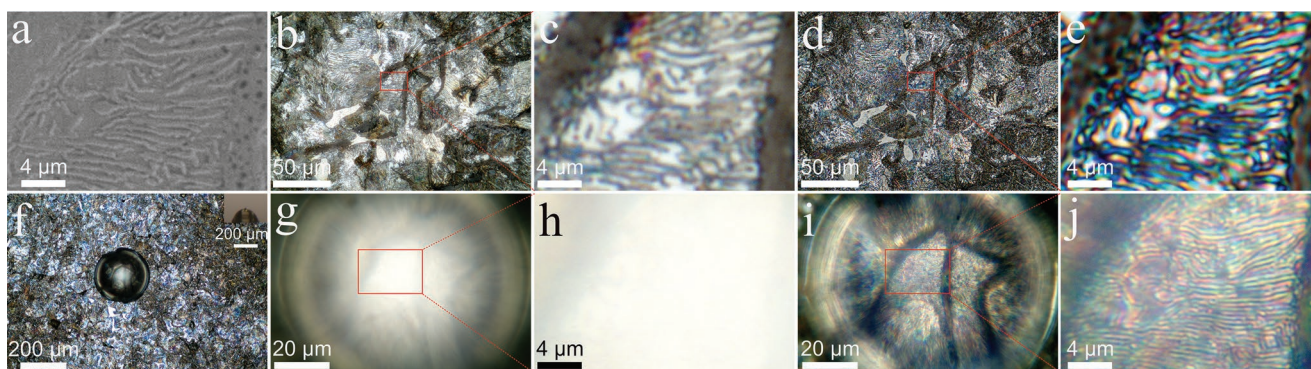
Figure 4. TiO$_2$ SIL used for super-resolution metallographic observation. a) SEM image of the pearlite lamellar microstructure. b–e) Transmission optical micrographs of the pearlite surface observed by the metallographic microscope using a 50× objective lens (NA = 0.8) under b) bright-field vertical illumination or d) bright-field oblique illumination, where (c) and (e) are enlarged images of (b) and (d), respectively. f) Optical micrographs of the top and side views of a TiO$_2$ SIL with a width of 188 μm and a height-width ratio of 0.60 used to observe the pearlite surface. g–j) Microscopic observations in combination with the TiO$_2$ SIL under g) bright-field vertical illumination or i) bright-field oblique illumination, where (h) and (j) are enlarged images of (g) and (i), respectively.

To further validate the super-resolution imaging capability of the TiO$_2$ SIL, a pearlite microstructure was examined under the metallographic optical microscope with a 50× objective lens (NA = 0.8). **Figure 4** compares the reflection optical micrographs of the pearlite microstructure observed at different microscopic illumination conditions. SEM image in Figure 4a shows that the pearlite has a dual-phase microstructure in which thin layers of ferrite and cementite are alternately arranged. The interlamellar spacing of pearlite is the average distance between two adjacent cementite lamellae, with a spacing of ≈150 nm. In the case of the direct microscope observation (Figure 4b) or combined the use of a TiO$_2$ SIL with a width of 188 μm and a height-width ratio of 0.60 (as shown in Figure 4f and its 2.4× magnified image in Figure 4g) under bright-field vertical illumination, the image quality is limited by low image contrast, as also seen in their enlarged views in Figures 4c and 4h, respectively. This is probably due to the high reflectivity of the metal surface leading to an overexposure of the observed structures and thus reducing the signal-to-noise ratio of the image. On the other hand, the use of bright-field oblique illumination under direct microscope observation can enhance the image contrast but is still insufficient to resolve the fine lamellar nanostructure of the pearlite, as shown in Figure 4d and its enlarged view in Figure 4e. However, through a combination of the TiO$_2$ SIL and the bright-field oblique illumination, the parallel alternating lamellae of ferrite and cementite as well as the interlamellar spacing of the pearlite were clearly observed in relatively high contrast, as shown in Figure 4i and the corresponding enlarged view in Figure 4j. These results further indicate that the oblique illumination can enhance the image resolution and contrast of the TiO$_2$ SIL, probably due to an improvement in signal-to-noise ratio was achieved. The optical performance of the TiO$_2$ SIL was compared with other SILs from the literature (Table S1, Supporting Information). The combination of microscope objective (e.g., 50×, NA = 0.8) and TiO$_2$ SIL has effectively increased the NA to around 1.83, which is one of the main factors that affect the depth of focus. In principle, the increase of NA can lead to shallower focal depth while improving the axial resolution. This is advantageous for eliminating distracting details in the background. However, the deeper focal depth is still achievable by using an aperture diaphragm in the optical path. It brings the user more flexibility in different scenarios.

In the above microscopic observations, the TiO$_2$ SIL was positioned directly on the material surface. As a result, the flat and smooth bottom surface of the TiO$_2$ SIL, which was directly obtained from the supporting polycarbonate film (Figure S8, Supporting Information), was in close proximity to the sample surface. This may facilitate the collection of near-field evanescent information. However, for the observation of many biological cells and tissues, a thin coverslip is always applied over the top of the balsam-mounted or water-suspended biological samples, which prevents the direct contact and focusing of the microlens to the samples. Here, we demonstrate that by replacing the conventional glass coverslip (typically with a thickness of 130 to 170 μm) with an ultrathin transparent plastic film (e.g., a 25-μm thick FEP film) to facilitate the focusing of the TiO$_2$ SIL on the underlying biological samples, it is also possible to improve the imaging resolution and contrast in real-time. In addition, the use of this ultra-thin coverslip was found to increase the imaging magnification factor of the TiO$_2$ SIL (Figure S9, Supporting Information).

Cancer is among the leading cause of death to human beings globally. So far, histopathological microscopic examination is still a gold standard for the diagnosis of various types of cancers in clinical practice, and an accurate differential diagnosis of cancer is very important to determine the optimal treatment strategy and thus improve the survival rate of patients.[1] **Figure 5** compares the optical micrographs of hematoxylin and eosin (H&E) stained cancer cells mounted with neutral balsam and then a 25-μm thick FEP coverslip, without or with focusing by a TiO$_2$ SIL under the 40× objective lens (NA = 0.75) of the transmission optical microscope, respectively. Figure 5a,b respectively show the direct microscopic observation of an H&E-stained histological section of human lung cancer tissue and its partially enlarged view. After transferring a TiO$_2$ SIL with a width of 630 μm and a height-width ratio of 0.562 onto the FEP coverslip surface, the ultrastructural details of the cell components such as nucleus and cytoplasm can be observed at higher resolution and contrast through the 3.0× magnified image (Figure 5c). For example, as respectively indicated by the
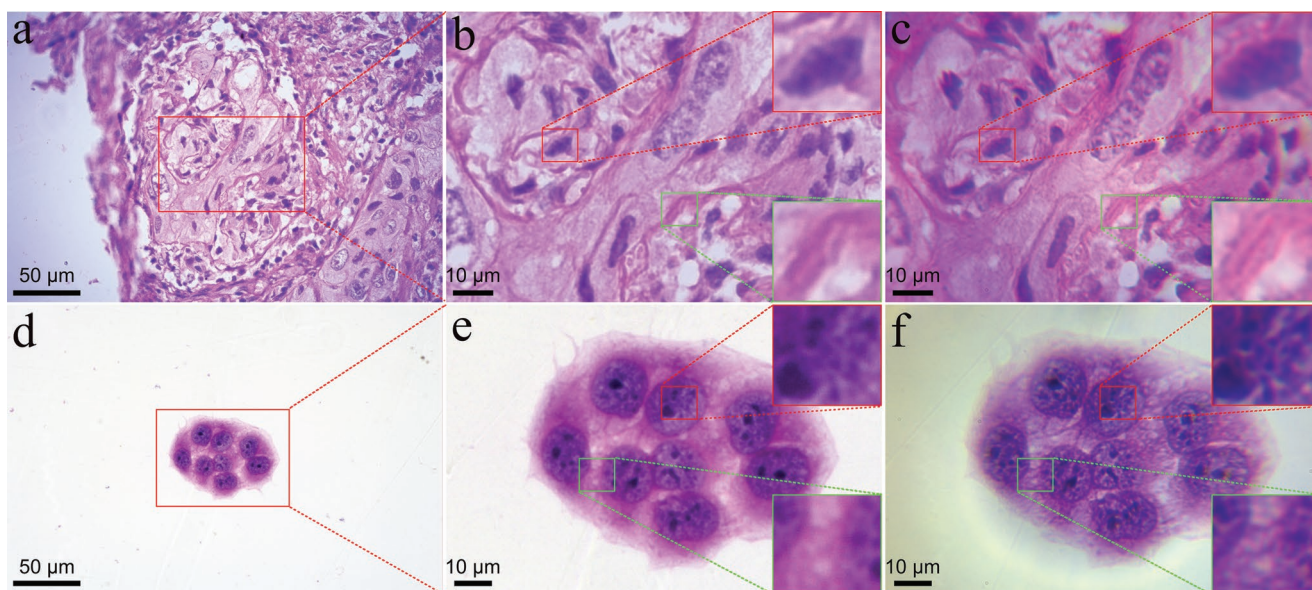
Figure 5. TiO$_2$ SIL used for microscopic pathological examination of H&E-stained cancer cells. a) An H&E-stained section of human lung cancer tissue or d) HeLa cells was directly observed under the 40× objective lens (NA = 0.75) of the transmission optical microscope, respectively. (b) and (e) are the partially enlarged views of (a) and (d), respectively. c,f) The corresponding cancer cells were observed through a TiO$_2$ SIL with a width of 630 µm and a magnification factor of 3.0, and a width of 578 µm and a magnification factor of 2.6, respectively. It can be seen that the TiO$_2$ SIL facilitates the observation of fine structural details of the nucleus and cytoplasm in the investigated cancer cells, as compared to the red and green boxes, respectively.

red and green boxes in Figure 5b,c, the irregularly distributed coarsely granular chromatin in the nuclei of cancer cells, as well as the filamentous structures in the cytoplasm were more obvious when using the microlens.

Furthermore, in Figure 5d, the morphological appearance of H&E-stained HeLa cells can be directly observed by the 40× objective lens. Its partially enlarged view in Figure 5e indicates that the HeLa cells have an oval-shaped nucleus, in which the central nucleolus is surrounded by a diffuse chromatin network. In addition, the cytoplasm of HeLa cells was observed composed of a filamentous network. However, through the 2.6× magnified image of a TiO$_2$ SIL with a width of 578 µm and a height-width ratio of 0.563, the chromatin condensation appears to have sharper outlines and well-defined borders, and the highly oriented filamentous units connected between two adjacent nuclei are also more clearly visible, as compared in the red and green dotted boxes in Figure 5e,f, respectively.

By using the ultrathin coverslip, the TiO$_2$ SIL also offers a non-invasive and real-time approach to observing living and unstained biological specimens immersed in an aqueous environment. For example, **Figure 6** compares the difference in microscopic morphology of various aqueous samples containing spiral bacteria (Figure 6a–c), *Streptococcus thermophilus* (Figure 6d–f), diatoms (Figure 6g–i), crenated mouse erythrocytes (Figure 6j–l), and normal mouse erythrocytes (Figure 6m–o) covered with a 25-µm thick FEP coverslip, and without or with using a TiO$_2$ SIL under the 40× objective lens (NA = 0.75) of the transmission optical microscope, respectively. Figure 6c,f,i,l,o respectively shows the entire FOV of the 2.5×, 3.5×, 3.5×, 3.2×, and 3.7× magnified images focused through a TiO$_2$ SIL with a width of around 600 µm. Compared to the direct observation through the 40× objective lens as respectively shown in Figure 6a,d,g,j,m, the tiny cells imaged with the TiO$_2$ SIL can occupy a significantly larger portion of the visual field, which will facilitate the precise identification of the detailed cellular structures.

Moreover, in comparison to the corresponding partially enlarged views of the direct observation as respectively shown in Figure 6b,e,h,k,n, the TiO$_2$ SIL can provide better image quality, as well as a 3D relief-like appearance, which can contribute to highlight the important characteristics of cellular structures, as shown in the red boxes, respectively. For example, the 40× objective lens is difficult to identify the characteristic spiral structure of the spiral bacteria due to the intrinsic low image contrast of bright-field microscopy for observing small and unstained cells. However, through the FOV of the TiO$_2$ SIL, it can be successfully captured that the spiral bacteria are helical in shape, even though the targets are moving rapidly across the visual field (Movie S1, Supporting Information). In addition, the TiO$_2$ SIL can more clearly show that the streptococcus thermophilus are spherical cocci arranged in chains (Movie S2, Supporting Information), the crenated mouse erythrocytes have several regularly spaced blunted projections protruding from the cell membrane (Movie S3, Supporting Information), the normal mouse erythrocytes typically with a biconcave discoid shape exhibit a distinct color contrast between the central depression and the elevated rounded edge of the erythrocytes, and the diatoms have parallel striae arranged at regular intervals, as indicated by the red boxes, respectively. These results suggest that the TiO$_2$ SIL can generate images of high-magnification and high-resolution suitable for visualization of delicate structures of low contrast or unstained biological specimens. Therefore, the TiO$_2$ SIL may offer a rapid and inexpensive way to facilitate the identification and diagnosis of infectious diseases such as bacterial infections, especially in medically underserved areas.
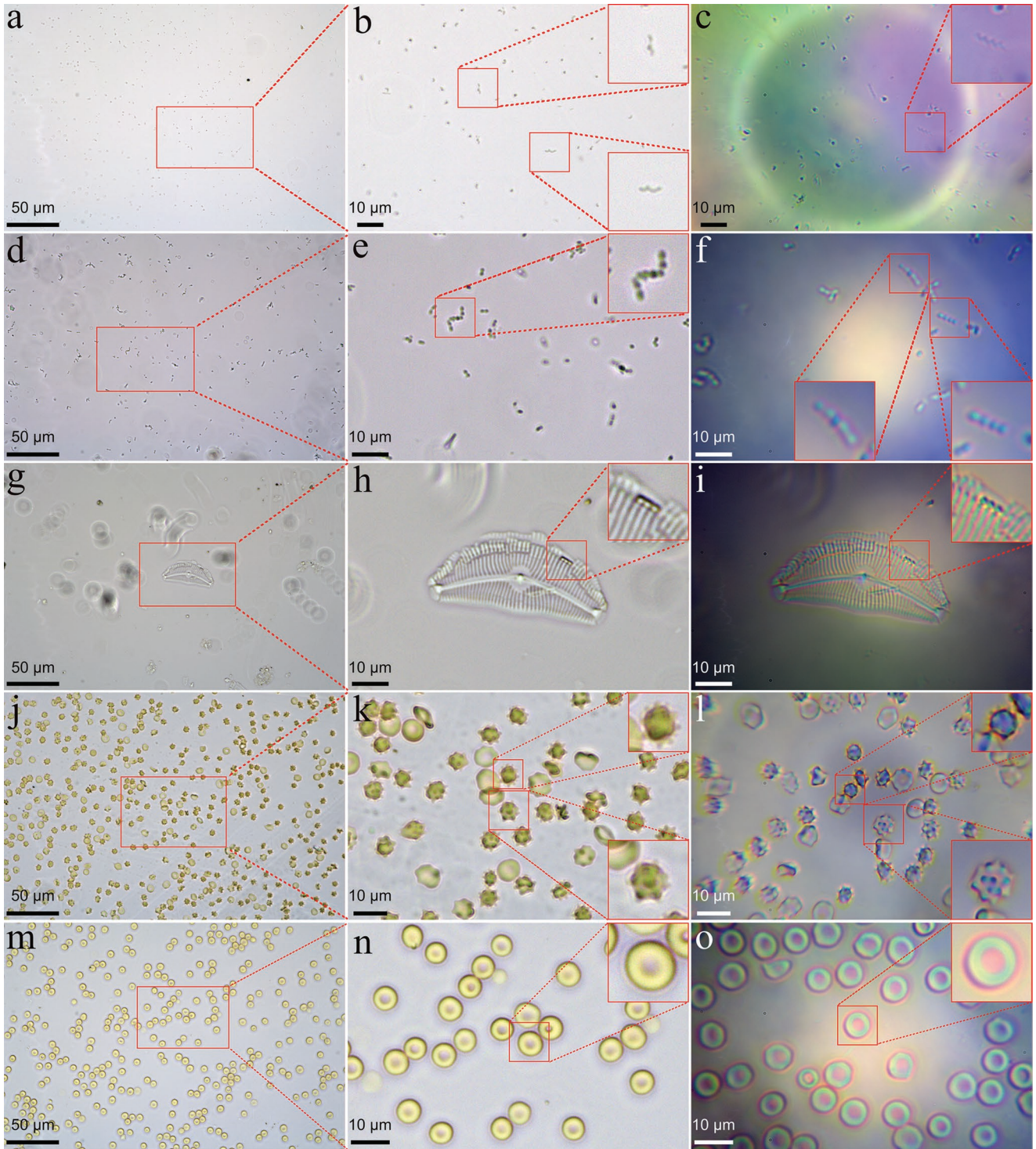
Figure 6. TiO$_2$ SIL used for real-time observation of living biological cells in an aqueous environment. a) spiral bacteria, d) streptococcus thermophilus, g) diatoms, j) crenated mouse erythrocytes, and m) normal mouse erythrocytes were immersed in water and directly observed under the 40× objective lens (NA = 0.75) of the transmission optical microscope, respectively. (b), (e), (h), (k), and (n) are the partially enlarged views of (a), (d), (g), (j), and (m), respectively. (c), (f), (i), (l), and (o) are the corresponding biological specimens observed through a TiO$_2$ SIL with a width of around 600 μm and a magnification factor of 2.5×, 3.5×, 3.5×, 3.2×, and 3.7×, respectively.

Compared to the scanning microscopy imaging techniques such as NSOM, the competitive advantages of this TiO$_2$ SIL technique are that it can provide wide FOV microscopic imaging in real-time as well as easy of operation, which overcomes the limitations of NSOM that has small optical throughput and relies on a relatively complicated point-to-point scanning operation to
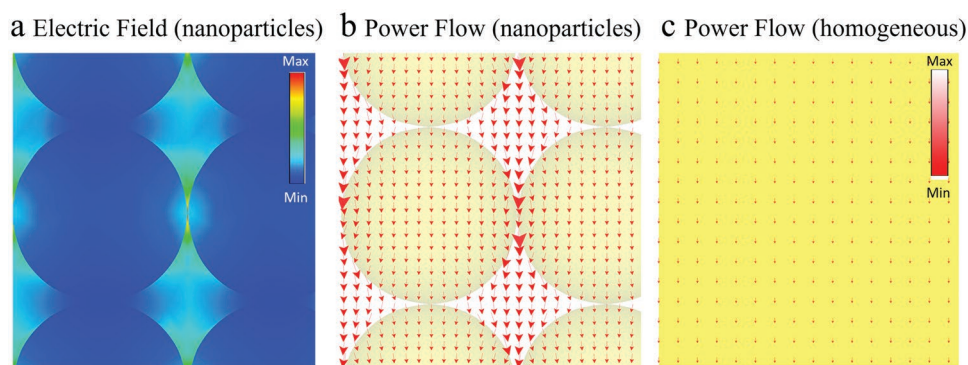
a Electric Field (nanoparticles) **b** Power Flow (nanoparticles) **c** Power Flow (homogeneous)

Figure 7. Simulation of electric field and power flow. a) Electric field distribution around the TiO$_2$ nanoparticle-assembled structure. Power flow of b) TiO$_2$ nanoparticle-assembled structure, and c) TiO$_2$ homogeneous material.

obtain a single fused image, and thus unsuitable for visualizing moving objects like living cells or bacteria.

2.4. Optical Simulation of TiO$_2$ SIL

Furthermore, to illustrate the physics of light interaction with TiO$_2$ nanoparticle composite in the TiO$_2$ SIL, a 3D full-wave simulation model was built based on a commercial software package (CST Microwave Studio). In **Figure 7**, field distribution and Poynting vector plots clearly show how light flows through the nanoparticle composite medium. Figure 7a shows the electric field distribution around 15 nm TiO$_2$ nanoparticles in the closely packed arrangement. Localized field enhancement is generated at the horizontal connection point between nanoparticles rather than the vertical connection. Therefore, incident light along the propagational direction is modulated and most of the light can pass through the material by vertically penetrating through the gaps. This is also verified by power flow results. The power flow plot records the Poynting vector in the same area, which depicts the direction and rate of transfer of energy. As can be seen in Figure 7b,c, the power flow is represented by red arrows and the size of the arrow represents the value of Poynting vector at this point. Comparing the two figures, we find that the artificial nano-assembled material has better light-guiding performance than the homogeneous material. In the homogeneous material, the light passes through it linearly without any influence. In the nano-assembled structure, light energy is amplified when it passes through a gap and then rapidly attenuated. Due to the small periodicity by 15 nm nanoparticle arrangement, the energy is amplified again before it has fully decayed, which could be the reason for its higher transmittance than homogeneous material. In addition, by comparing the calculated transmission/absorption/reflection spectra, we can see that high transparency can be maintained within the simulated nanoparticle composite medium and can even exceed the traditional homogeneous medium case (Figures S10 and S11, Supporting Information). The simulation results also reveal that compared to the perfect hexagonal arrangement, a small fraction of defects in the nanoparticle-assembled structure does not influence the optical performance, which

is important for maintaining repeatability in the experiments (Figure S12, Supporting Information).

3. Conclusion

In summary, by using the silicone oil two-step dehydration method, high-refractive-index 15 nm TiO$_2$ nanoparticles have been assembled into TiO$_2$ SILs with highly dense micro-structures and controllable macroscopic shapes, which is not available from other top-down or bottom-up fabrication methods. This TiO$_2$ nanoparticle-assembled SIL with a high refractive index and transparency is highly desirable to visualize microscopic structures with improved image magnification, resolution, and contrast under a conventional transmission or reflection light microscope. The sub-millimeter-sized SIL overcomes the shortcomings of previous micron-scale hemispherical or spherical superlens that suffered from limited FOV and difficulty in manipulation and thereby provides a significantly wider FOV as well as ease of operation which is necessary for the precise location of the FOV. Moreover, the TiO$_2$ SIL can be easily and cost-effectively fabricated on large scales without the use of sophisticated equipment or techniques. This TiO$_2$ SIL can provide a practical and diverse tool for the observation of sub-diffraction-limited details of nanomaterials, and the accurate histological examination of cancer tissues, as well as the real-time identification of specific subcellular structures in unstained living cells and bacteria, which are hardly detectable by conventional optical microscopes. The TiO$_2$ SIL may also be applicable to other important SIL-related applications, such as photolithography, high-density optical data storage, and semiconductor-integrated optical devices.[38] Finally, the further integration of the TiO$_2$ SIL with an AFM-like automated positioning system may provide a high-resolution strategy for high-throughput optical scanning microscope, for example, automated whole slide imaging and digital image analysis in cancer diagnosis.[41–43]

4. Experimental Section

Purification of TiO$_2$ Nanoparticles: The aqueous dispersion of anatase TiO$_2$ nanoparticles with an average particle size of 15 nm, a zeta

potential of +27 mV, and a solid content of 15 wt% was purchased from Hangzhou Wanjing New Materials Co. Ltd., China. The aqueous dispersion was centrifuged at 10 000 g for 30 min to remove the large agglomerates. The resulting supernatant with a solid content of about 12 wt% was collected and used for further experiments.

Preparation of Test Specimens: In Figure 3, the 400 nm SiO_2 nanospheres were purchased from Huge Biotechnology. Co. Ltd., China. The 300 nm polystyrene (PS) nanospheres were purchased from Wuxi Knowledge & Benefit Sphere Tech. Co. Ltd., China. The SiO_2 or PS nanospheres were assembled into a close-packed monolayer on a polydimethylsiloxane (PDMS) substrate according to a friction method reported in the literature.[39] In Figure 5, the commercially available hematoxylin and eosin (H&E) stained pathology slides for teaching and research purposes were obtained from commercial suppliers. To remove the original 170 μm thick coverslip from the glass slides, the slides were immersed in xylene until the coverslip could be removed. Then, the cells that remained on the glass slides were mounted with neutral balsam with a refractive index of 1.52 and subsequently covered by a 25-μm thick fluorinated ethylene-propylene (FEP) transparent film as an ultrathin coverslip. In Figure 6, the spiral bacteria were collected from lake water, the diatoms were collected from the Huangpu River, the streptococcus thermophilus were obtained from commercially available products, and the blood samples containing erythrocytes were taken from the tail vein blood of a laboratory mouse and subsequently diluted with normal saline (1:2 ratio) before use. These aqueous biological samples were respectively dropped onto a glass slide and then covered by a 25-μm thick FEP coverslip before microscopic observation. In Figure 6m–o, the normal erythrocytes were observed immediately after sample preparation. To obtain the crenated erythrocytes in Figure 6j–l, the normal erythrocyte sample was left standing at room temperature of 25 °C for about 10 min. The gradual evaporation of water from the blood along the edge of the FEP coverslip can produce a hypertonic extracellular environment, causing the erythrocytes to shrink and exhibit a crenated appearance. Ethical approval was granted by the ethics committee of Hubei University.

Fabrication of TiO₂ SIL: The TiO₂ SIL was fabricated by a self-assembly method described by the authors with some modifications.[40] First, 40 ml silicone oil was added to a 9-cm-diameter glass Petri dish and subsequently, a 4×3 cm polycarbonate thin film was placed onto the bottom surface of the Petri dish. Then, a certain volume of TiO₂ aqueous dispersion was added to the polycarbonate film using a pipette. The droplet of TiO₂ aqueous dispersion was completely immersed in silicone oil and deformed into a hemispherical shape. The Petri dish without the cover was then heated in an oven without forced air circulation at 70 °C for ≈1–2 h. After completing the first step of dehydration, the silicone oil was removed from the Petri dish using a Pasteur pipette, followed by the second step of dehydration by keeping the Petri dish at a room temperature of 25 °C for 24 h. Finally, a transparent solid TiO₂ microlens with a regular hemispherical shape can be fabricated and the residual silicone oil on the lens surface was cleaned with hexane or absorbent paper. TiO₂ SIL with different widths and height-width ratios can be fabricated by varying the experimental parameters (Figure S13, Supporting Information).

SEM Observation: The surface morphology of the samples was observed using an SEM (Zeiss Sigma 500) after gold coating.

Optical Microscope Observation: The transmission optical micrographs were taken using a transmission optical microscope (Nikon Eclipse Ci-L) equipped with a 20-megapixel CMOS camera, a white light source, and a 10× objective lens (Nikon Plan, NA = 0.25, working distance: 10.5 mm) or a 40× objective lens (Nikon Plan Fluor, NA = 0.75, working distance: 0.66 mm), in either bright-field vertical illumination or dark-field oblique illumination modes through a dark-field condenser (Nikon Phase Contrast). The reflection optical micrographs were taken using a metallographic optical microscope (Nikon Eclipse LV-100) equipped with a 32-megapixel CMOS camera, a white light source, and a 50× objective lens (Nikon LU Plan Fluor, NA = 0.8, working distance: 1.0 mm) or a 100× objective lens (Nikon LU Plan Fluor, NA = 0.9, working distance:

1.0 mm), in either bright-field vertical illumination or bright-field oblique illumination modes through a physical filter.

Supporting Information

Supporting Information is available from the Wiley Online Library or from the author.

Conflict of Interest

The authors declare no conflict of interest.

Data Availability Statement

The data that support the findings of this study are available from the corresponding author upon reasonable request.

Keywords

nano self-assembly, solid immersion lens, super-resolution optical microscopy, titanium dioxide nanoparticles

[1] E. Balaur, O. T. S. , A. J. Spurling, G. B. Mann, B. Yeo, K. Harvey, C. Sadatnajafi, E. Hanssen, J. Orian, K. A. Nugent, B. S. Parker, B. Abbey, *Nature* **2021**, *598*, 65.

[2] Y. Baek, Y. Park, *Nat. Photonics* **2021**, *15*, 354.

[3] Y. Zhou, H. Zheng, I. I. Kravchenko, J. Valentine, *Nat. Photonics* **2020**, *14*, 316.

[4] Z. Hu, X. Huang, Z. Yang, J. Qiu, Z. Song, J. Zhang, G. Dong, *Light: Sci. Appl.* **2021**, *10*, 140.

[5] X. Xi, J. Ma, S. Wan, C.-H. Dong, X. Sun, *Sci. Adv.* **2021**, *7*, abe1398.

[6] W. Fan, J. Zeng, Q. Gan, D. Ji, H. Song, W. Liu, L. Shi, L. Wu, *Sci. Adv.* **2019**, *5*, aaw8755.

[7] X. Wen, B. Zhang, W. Wang, F. Ye, S. Yue, H. Guo, G. Gao, Y. Zhao, Q. Fang, C. Nguyen, X. Zhang, J. Bao, J. T. Robinson, P. M. Ajayan, J. Lou, *Nat. Mater.* **2021**, *20*, 1506.

[8] Y. C. Liu, K. Huang, X. Y. F. , *Natl. Sci. Rev.* **2021**, *8*, nwaa210.

[9] X. Hao, C. Kuang, Z. Gu, Y. Wang, S. Li, Y. Ku, Y. Li, J. Ge, X. Liu, *Light: Sci. Appl.* **2013**, *2*, 108.

[10] L. Schermelleh, A. Ferrand, T. Huser, C. Eggeling, M. Sauer, O. Biehlmaier, G. P. C. Drummen, *Nat. Cell Biol.* **2019**, *21*, 72.

[11] Y. M. Sigal, R. Zhou, X. Zhuang, *Science* **2018**, *361*, 880.

[12] Z. Yang, A. Sharma, J. Qi, X. Peng, D. Y. Lee, R. Hu, D. Lin, J. Qu, J. S. Kim, *Chem. Soc. Rev.* **2016**, *45*, 4651.

[13] R. Kato, T. Moriyama, T. Umakoshi, T. A. Yano, P. Verma, *Sci. Adv.* **2022**, *8*, abo4021.

[14] K. Frischwasser, K. Cohen, J. Kher-Alden, S. Dolev, S. Tsesses, G. Bartal, *Nat. Photonics* **2021**, *15*, 442.

[15] G. Hu, Q. Ou, G. Si, Y. Wu, J. Wu, Z. Dai, A. Krasnok, Y. Mazor, Q. Zhang, Q. Bao, C. W. Qiu, A. Alu, *Nature* **2020**, *582*, 209.

[16] S. S. Sunku, G. X. Ni, B. Y. Jiang, H. Yoo, A. Sternbach, A. S. McLeod, T. Stauber, L. Xiong, T. Taniguchi, K. Watanabe, P. Kim, M. M. Fogler, D. N. Basov, *Science* **2018**, *362*, 1153.

[17] N. Fang, H. Lee, C. Sun, X. Zhang, *Science* **2005**, *308*, 534.

[18] Z. Liu, H. Lee, Y. Xiong, C. Sun, X. Zhang, *Science* **2007**, *315*, 1686.

[19] W. J. Padilla, R. D. Averitt, *Nat. Rev. Phys.* **2021**, *4*, 85.

[20] Z. Wang, W. Guo, L. Li, B. S. Luk'yanchuk, A. Khan, Z. Liu, Z. Chen, M. Hong, *Nat. Commun.* **2011**, *2*, 218.

[21] F. Wang, L. Liu, H. Yu, Y. Wen, P. Yu, Z. Liu, Y. Wang, W. J. Li, *Nat. Commun.* **2016**, *7*, 13748.

[22] X. Luo, *Adv. Mater.* **2019**, *31*, 1804680.

[23] W. Fan, B. Yan, Z. Wang, L. Wu, *Sci. Adv.* **2016**, *2*, 1600901.

[24] H. Zhu, W. Fan, S. Zhou, M. Chen, L. Wu, *ACS Nano* **2016**, *10*, 9755.

[25] J. Rho, Z. Ye, Y. Xiong, X. Yin, Z. Liu, H. Choi, G. Bartal, X. Zhang, *Nat. Commun.* **2010**, *1*, 143.

[26] D. Lu, Z. Liu, *Nat. Commun.* **2012**, *3*, 1205.

[27] S. Kwon, J. Park, K. Kim, Y. Cho, M. Lee, *Light: Sci. Appl.* **2022**, *11*, 32.

[28] X. Chen, T. Wu, Z. Gong, J. Guo, X. Liu, Y. Zhang, Y. Li, P. Ferraro, B. Li, *Light: Sci. Appl.* **2021**, *10*, 242.

[29] Y. Li, H. Xin, Y. Zhang, H. Lei, T. Zhang, H. Ye, J. J. Saenz, C. W. Qiu, B. Li, *ACS Nano* **2018**, *12*, 10703.

[30] Y. Yan, L. Li, C. Feng, W. Guo, S. Lee, M. Hong, *ACS Nano* **2014**, *8*, 1809.

[31] L. Li, W. Guo, Y. Yan, S. Lee, T. Wang, *Light: Sci. Appl.* **2013**, *2*, 104.

[32] R. Dhama, B. Yan, C. Palego, Z. Wang, *Photonics* **2021**, *8*, 222.

[33] A. Bogucki, L. Zinkiewicz, M. Grzeszczyk, W. Pacuski, K. Nogajewski, T. Kazimierczuk, A. Rodek, J. Suffczynski, K. Watanabe, T. Taniguchi, P. Wasylczyk, M. Potemski, P. Kossacki, *Light: Sci. Appl.* **2020**, *9*, 48.

[34] Y. Kutovyi, M. M. Jansen, S. Qiao, C. Falter, N. von den Driesch, T. Brazda, N. Demarina, S. Trellenkamp, B. Bennemann, D. Grutzmacher, A. Pawlis, *ACS Nano* **2022**, *16*, 14582.

[35] L. Wang, B. Bateman, L. C. Zanetti-Domingues, A. N. Moores, S. Astbury, C. Spindloe, M. C. Darrow, M. Romano, S. R. Needham, K. Beis, D. J. Rolfe, D. T. Clarke, M. L. Martin-Fernandez, *Commun. Biol.* **2019**, *2*, 74.

[36] C. Toninelli, I. Gerhardt, A. S. Clark, A. Reserbat-Plantey, S. Gotzinger, Z. Ristanovic, M. Colautti, P. Lombardi, K. D. Major, I. Deperasinska, W. H. Pernice, F. H. L. Koppens, B. Kozankiewicz, A. Gourdon, V. Sandoghdar, M. Orrit, *Nat. Mater.* **2021**, *20*, 1615.

[37] D. Kang, C. Pang, S. M. Kim, H. S. Cho, H. S. Um, Y. W. Choi, K. Y. Suh, *Adv. Mater.* **2012**, *24*, 1709.

[38] B. S. Luk'yanchuk, R. Paniagua-Domínguez, I. Minin, O. Minin, Z. Wang, *Opt. Mater. Express* **2017**, *7*, 1820.

[39] C. Park, T. Lee, Y. Xia, T. J. Shin, J. Myoung, U. Jeong, *Adv. Mater.* **2014**, *26*, 4633.

[40] W. Fan, L. Wu, *J. Inorg. Mater.* **2018**, *33*, 1337.

[41] M. Duocastella, F. Tantussi, A. Haddadpour, R. P. Zaccaria, A. Jacassi, G. Veronis, A. Diaspro, F. D. Angelis, *Sci. Rep.* **2017**, *7*, 3474.

[42] A. Jacassi, F. Tantussi, M. Dipalo, C. Biagini, N. Maccaferri, A. Bozzola, F. D. Angelis, *ACS Appl. Mater. Interfaces* **2017**, *9*, 32386.

[43] Y. Rivenson, A. Ozcan, *Light: Sci. Appl.* **2022**, *11*, 300.